Journal of Materials Chemistry A

Materials for energy and sustainability

rsc.li/materials-a

ROYAL SOCIETY
OF **CHEMISTRY**

10 YEARS ANNIVERSARY
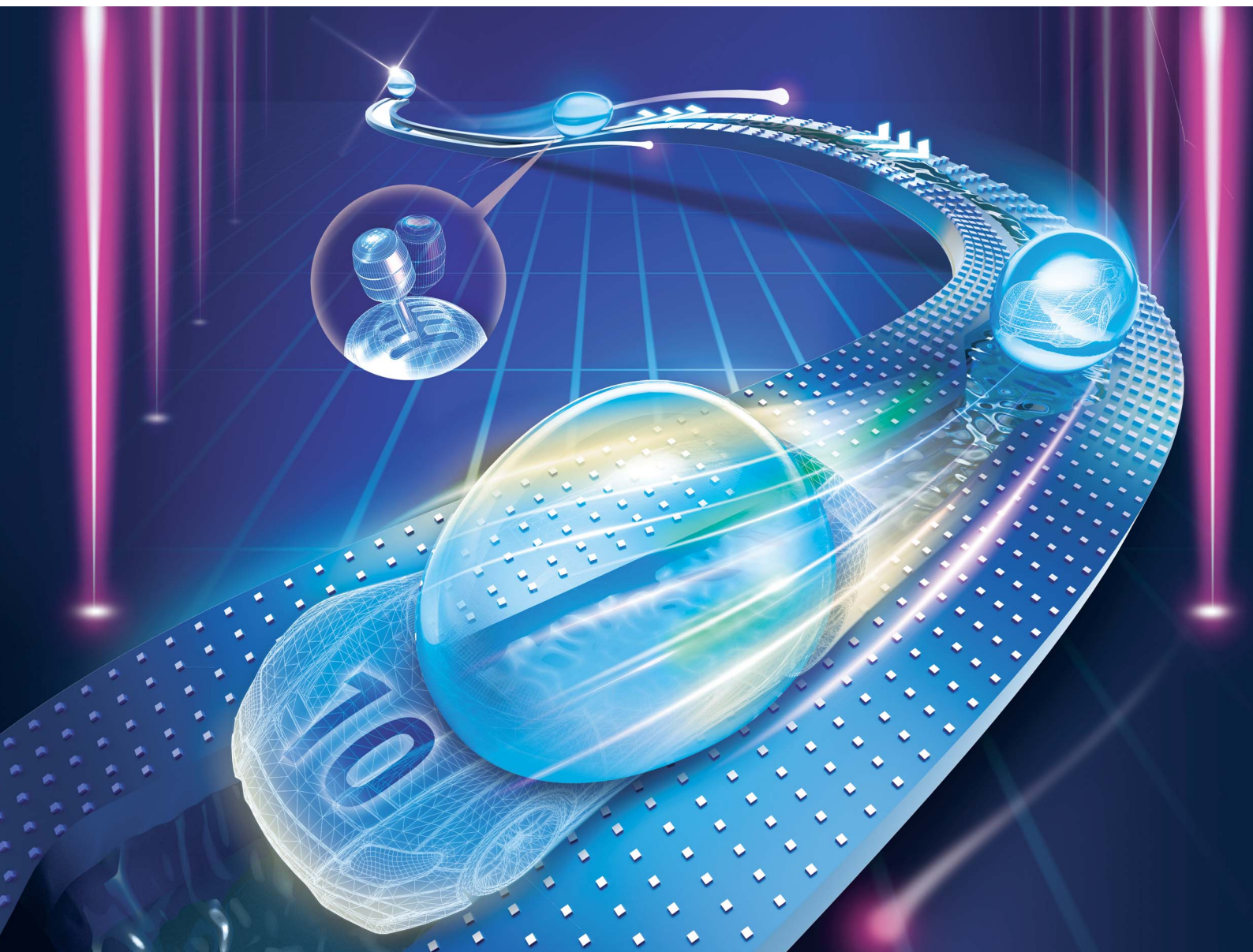
PAPER
Xiuqing Hao *et al.*
Achieving ultralong directional liquid transportation
spontaneously with a high velocity

ROYAL SOCIETY
OF CHEMISTRY

PAPER

Achieving ultralong directional liquid transportation spontaneously with a high velocity†

Qiankai Liu,‡[a] Jie Zhang,‡[a] Pengcheng Sun,‡[ab] Jianping Wang,[a] Wei Zhao,[a] Guolong Zhao,[a] Ni Chen,[a] Yinfei Yang,[a] Liang Li,[a] Ning He,[a] Zuankai Wang[c] and Xiuqing Hao ✩ *[a]

Due to its appeal in the merit of no external energy input, the passive surface is widely considered to be an ideal platform for liquid transportation. Despite the considerable progress attained, achieving long-range and high-speed liquid transport on a passive surface remains challenging due to several inherent difficulties, such as the insufficient driving force and undesired energy dissipation. Here, we overcome these limitations by proposing a cellular design of wettability pattern (CWP). This CWP is composed of cells with a wettability gradient and a cascaded super-hydrophilic divergent channel, where the cells are seamlessly interconnected with each other through the channel. Utilizing the enhanced driving force and reduced energy dissipation endowed by the special wetting and geometrical design, the proposed CWP can spontaneously transport a water droplet over a distance of 100 mm, the longest distance ever reported, with a high average velocity of $\sim$92 mm s^{-1}. We demonstrate experimentally and theoretically that the transport distance can be further enhanced by tailoring the wettability gradient. Using a predefined CWP, we also achieve on-demand liquid manipulation. We envision that our cellular design will find numerous applications in materials science, interfacial chemistry, and biomedical research.

1. Introduction

Liquid transport has practical applications in numerous fields, such as microfluidics, water harvesting, and heat transfer devices.[1–7] Liquid transport is mainly classified into active and passive transport. However, the complex manufacturing technology and inherent energy waste hinder the application of active liquid transport.[8–13] On the other hand, as it does not require any external energy input, the passive surface is widely considered to be an ideal platform for liquid transport. Through natural selection, some animals and plants have evolved unique functional surfaces for liquid passive transport. These include the reed leaf,[14] pitcher plant,[15] cacti,[16,17] Sarracenia,[18] and spider silk.[1] The exceptional passive transport characteristics of these structures are induced by the asymmetry of the chemical components or morphology, which breaks the symmetricity of the contact line and thus generates the driving force for liquid

transportation.[19–28] Taking inspiration from these natural phenomena, many researchers have conducted in-depth studies on liquid transportation.[18,25,29,30] For instance, based on the ultrafast water harvesting and transportation mechanism of Sarracenia trichome, Chen *et al.* reported the fabrication of artificial bio-inspired hierarchical microchannels *via* photolithography. These channels could achieve continuous water harvesting with an average velocity v_a of up to $\sim$7 mm s^{-1} and a maximal transportation distance L_{max} of up to $\sim$13 mm.[18] Inspired by the grooved structures of the rice leaf and the wedge-shaped structures of the shorebird beak, Lu *et al.* reported a wedge-shaped grooved nanotextured slippery liquid-infused porous surface to confine the droplet footprint and squeeze the droplet in order to obtain a Laplace pressure difference for continuous self-driven droplet transport.[25] Although continuous self-driven transportation has been successfully demonstrated in biomimetic channels, it is still affected by numerous disadvantages, including limited transportation velocity and short transportation distance. To enhance droplet transportation, patterned surfaces have been widely adopted due to the strong driving force induced by the Laplace pressure difference.[16,31–40] For instance, Zheng *et al.* proposed a method based on a vein-like shape to realize the directional transportation of water on a super-hydrophobic surface[38] ($L_{max} \approx 40$ mm, $v_a \approx 20$ mm s^{-1}). However, for a single-wedge-shaped wettability pattern, when drops are transported to the end of the pattern, the terminal size of the

[a] College of Mechanical and Electrical Engineering, Nanjing University of Aeronautics & Astronautics, Nanjing, 210016, China. E-mail: xqhao@nuaa.edu.cn; zk.wang@polyu.edu.hk

[b] Department of Mechanical Engineering, City University of Hong Kong, Hong Kong, 999077, China

[c] Department of Mechanical Engineering, The Hong Kong Polytechnic University, Hong Kong, 999077, China

‡ These authors are co-first authors.

10164 | *J. Mater. Chem. A*, 2023, **11**, 10164–10173

This journal is © The Royal Society of Chemistry 2023

pattern for long-distance transportation is large. This leads to a sharp decrease in the inner Laplace pressure difference, which implies that the single-wedge-shaped channel cannot be used for long-distance transportation. Furthermore, Song *et al.* developed a patterned surface with a serial-wedge-shaped channel, which is composed of several single-wedge-shaped channels connected in series.[41] Different from the transportation on the single-wedge-shaped channel, a sufficiently high inner Laplace pressure difference and a high transportation velocity can be maintained for long-distance droplet transportation. Furthermore, the width of the wide side of the channel is independent of its length, which is beneficial to reduce the mass loss caused by spreading transportation and enhance the transportation distance. Specifically, once a drop moves to a junction of the serial-wedge-shaped channel, the drop encounters energy barriers induced by the hysteresis effect and thus decelerates rapidly, and its transportation distance is thus considerably limited.

Further, to help drops pass smoothly through junctions, additional drive methods have been introduced into channels as a viable idea to improve droplet transport performance. For instance, Feng *et al.* developed a multi-conical wettability gradient surface, which could significantly improve the water collection efficiency.[42] Specifically, when drops move to the junctions of multiple cones, they pass smoothly due to the combined action of the Laplace pressure difference and the wettability gradient. The establishment of a wettability gradient induced by a surface energy gradient is an approach that has been widely used for drop transportation. However, the transportation performance is poor if the wettability gradient is used as the sole driving force.[21,43–47] Therefore, conical or wedge-shaped channels have been combined with the wettability gradient by some researchers to optimize the droplet transportation capacity.[48–50] For instance, Li *et al.* realized a wettability gradient (from 64.6° to 18.6°) in a wedge-shaped pattern on a copper substrate using the mask technique and chemical etching, which resulted in a drop transportation distance of up to 21.6 mm and an average transportation speed of 0.53 mm s^{-1}.[49] Rossegger *et al.* realized a wettability gradient (from 97° to 19°) in a wedge-shaped pattern on a photopolymer surface using the mask technique and irradiation, and the combination of the wettability gradient and the wedge-shaped structure enabled a rapid and directed movement of water droplets (2 μL) over a reasonable distance (up to 10 mm).[50] Though many different water transport strategies have been proposed, they result in either a low velocity or a short transportation distance, which hinders the application of water transport in practical settings. Therefore, it is necessary to develop a surface that can achieve long-range, directional, and high-velocity drop transportation.

In this study, a cellular design of wettability pattern (CWP), which is composed of a cascaded super-hydrophilic divergent channel and a gradient hydrophobic background consisting of cells with a wettability gradient, was fabricated through laser irradiation. This scheme enables ultralong directional drop transportation spontaneously with a high velocity. Specifically, the motion of a single drop on the CWP can be considered to be analogous to the motion of a car on a periodic downhill and uphill track, and the effect of the gradient hydrophobic background is similar to that of lowering the gear for a car moving uphill, which improves the driving force. Before preparing the CWP, we studied the influence of the laser scanning speed on the wettability, and the results regarding the preparation of gradient hydrophobic backgrounds are provided. Based on these experimental results, an appropriate gradient hydrophobic background was prepared, and a streamlined cascaded divergent channel was fabricated on it to form the CWP. A cascaded divergent channel on a uniform hydrophobic background (CDU) and a streamlined cascaded divergent channel on a uniform hydrophobic background (SDU) were also fabricated for comparison. The influence of the main parameters of the cascaded divergent channels and the gradient hydrophobic backgrounds on the transportation behavior at junctions was systemically studied. Furthermore, the effect of the average wettability gradient k on the drop transportation distance was explored, which is expected to enable the achievement of long-distance drop transportation. We envision that our cellular design will find broad applications in materials science, interfacial chemistry, and biomedical research.

2. Experimental section

2.1. Sample preparation

Before fabrication, a 6061 aluminum alloy sheet (120 mm × 20 mm × 5 mm) was first cleaned ultrasonically in absolute ethanol for 10 min. The processing of the surfaces consisted of two steps. In step one, the metal surface was hatched in both horizontal and vertical directions through direct laser writing, and this process was performed separately at the same scanning speed and at a gradient scanning speed. Subsequently, the engineered surface was immersed in a fluorinated solution (0.8 wt%, PFDTS, Sicong Chemical, China) for 10 min to decrease the surface energy and thus form uniform and gradient hydrophobic backgrounds, respectively. In step two, we prepared the cascaded divergent channel and the streamlined cascaded divergent channel on the uniform hydrophobic background (CDU and SDU, respectively) and fabricated a streamlined cascaded divergent channel on the gradient hydrophobic background (CWP). Notably, a gradient hydrophobic background consists of multiple cells seamlessly connected, where the contact angle inside each cell is the same, and the contact angle of the background decreases discretely along the transportation direction due to the decrease in the contact angle of the cells. The fabrication process of the CWP is shown in Fig. S1,† and the manufacturing process of the CDU and the SDU is similar to that of the CWP. The fabrication of CWPs with different average wettability gradients ($k = 0$, 0.20, 0.30, and 0.35° mm^{-1}) was achieved using different laser scanning speeds. The detailed laser parameters are shown in Tables S1 and S2.† Laser ablation was achieved using a nanosecond laser (SK-CX20, Sanke laser, China) with a wavelength of 1064 nm, a pulse width of 200 ns, a maximum power of 20 W, and a frequency ranging from 20 to 100 kHz.

2.2. Characterization

The surface morphology and three-dimensional (3D) profile were obtained using scanning electron microscopy (SEM, Quanta250FEG, FEI, US) and the confocal microscopy unit of a 3D Optical Profiler (Sneox, Sensofar, Spain), respectively. The surface chemical analysis was performed *via* energy-dispersive spectroscopy (Quanta 250 FEG, FEI, US). A Rhodamine B solution (1 wt%, Red, $C_{28}H_{31}ClN_2O_3$, Sinopharm, China) was used to measure the surface wettability and for the self-transport experiments. The contact angles and sliding angles of the drops were measured using a contact angle meter (OCA25HTV, Dataphysics, Germany), and each measurement was conducted at five different positions. The drop volume used in these measurements was 5 μL. Before the self-transport experiments, the channels needed to be pre-wetted, which was done to exclude the influence of the capillary phenomenon on droplet transport. Thus, a few drops (the volume of each drop was 5 μL) were dropped in advance to cover the super-hydrophilic groove. In addition, in the liquid identification experiment, four liquids to be identified were placed in four reservoirs in advance, and then an indicator (a 25 μL drop) was continuously transported from the starting end to the four reservoirs. The four liquids were a glucose solution (2 wt%, Colorless, $C_6H_{12}O_6$, Sinopharm, China), deionized water (Colorless), a sodium hydroxide solution (3 wt%, Colorless, NaOH, pH > 13, Sinopharm, China), and an indigo carmine solution (1 wt%, Blue, $C_{16}H_8N_2Na_2O_8S_2$, Sinopharm, China), which was used as the indicator in the identification experiment. The optical images were captured using a commercial camera (Sony α7, Japan) equipped with a microlens (SEL90M28G, Sony, Japan).

3. Results and discussion

To explore a surface that enables high-performance drop transportation, three surfaces have been designed, including CDU, SDU, and CWP. Fig. 1(a) shows the design concept of surfaces, which all consist of super-hydrophilic channels and hydrophobic backgrounds. A cascaded super-hydrophilic divergent channel on a uniform hydrophobic background (CDU) is proposed for long-distance liquid transportation.[41] This channel is different from the single-wedge-shaped channel,[51–54] where liquid residue appears on the transportation path. However, drops can be easily blocked at the junctions of the channel due to the large hysteresis resistance force generated by the rapid changes in the channel width. To reduce this force at the junctions, we developed a streamlined cascaded super-hydrophilic divergent channel with curved joints on a uniform hydrophobic background (SDU) by tuning the geometrical parameters. In this channel, the transportation distance of droplets is slightly increased. Furthermore, a CWP was fabricated using a laser, which is composed of a cascaded super-hydrophilic divergent channel and a gradient hydrophobic background consisting of cells with a wettability gradient. The transportation capacity of the CWP is higher than that of other reported structures due to the combined action of the Laplace pressure difference and the wettability gradient, as shown in Fig. 1(c).

For the CWP, the motion of a single drop on the surface can be considered to be analogous to the motion of a car on a periodic downhill and uphill track, as shown in Fig. 1(b). The drop first accelerates in the wedge-shaped region because of the Laplace pressure difference, which is similar to the downhill motion of the car. As the drop is transported to a junction, it decelerates rapidly due to the energy barrier, and the wettability gradient force generated by the gradient hydrophobic background aids the drop in smoothly passing through the junction. This process is similar to the uphill motion of the car. Specifically, when the car is at a low speed, the effect of the wettability gradient force is similar to that of lowering the gear, which enhances the car driving force. At this point, one cycle of motion of the drop/car is completed, and the drop/car reaches the endpoint of the track with a high velocity after multiple cycles. The gradient hydrophobic background of the CWP is crucial to improve the transport of droplets, and the wettability gradient arises from the change in the wettability of the cells. Taking the optimal gradient hydrophobic background in our study as an example, as shown in Fig. 1(d), the contact angle θ of the background decreases with increasing x, which is the transportation distance along the CWP. In this study, the change in wettability is achieved through the reconfiguration of the surface structure, which in turn is obtained by regulating the laser scanning speed. The relationship between the surface structure and the background wettability as well as the related analysis is shown in Fig. S2 and Table S3.†

To verify whether the optimization of the geometric parameters and the gradient hydrophobic background facilitates drop motion at junctions, the motion of a 25 μL drop at junctions of channels with various contact angle differences of the two backgrounds $\Delta\theta$ and geometric parameters was explored. The geometric parameters considered include the narrow-side width w_1, wide-side width w_2, half-wedge angle β_1, and transition angle β_2, which are shown in Fig. 2(e) and (f). As shown in Fig. 2(a) and Video S1,† for a junction with $\frac{w_1}{w_2} = 0.14$ and $w_2 = 1$ mm, the drop can pass through the SDU junction but is blocked at the CDU junction, which means that streamlined boundaries can assist drop motion through junctions. For a sharper junction with $\frac{w_1}{w_2} = 0$ and $w_2 = 1$ mm, the drop can pass through the CWP junction but is blocked at the SDU junction, as shown in Fig. 2(b) and Video S2,† which means that the gradient hydrophobic background helps the drop in passing through junctions. In particular, for specific β_1 and w_2 values, there is a critical width ratio $\frac{w_{1c}}{w_2}$ such that when $\frac{w_1}{w_2} \geq \frac{w_{1c}}{w_2}$, the drop can pass through junctions.[55] Furthermore, the effect of $\Delta\theta$ on the critical width ratio was investigated, and the value of the critical width ratio decreased with the increase in $\Delta\theta$, as shown in Fig. 2(c) and (d). This implies that drops can pass through junctions with a small width ratio due to the help of $\Delta\theta$, which enables small volumes of liquid to pass as drops at junctions, thereby enhancing the efficiency of liquid transport. For the
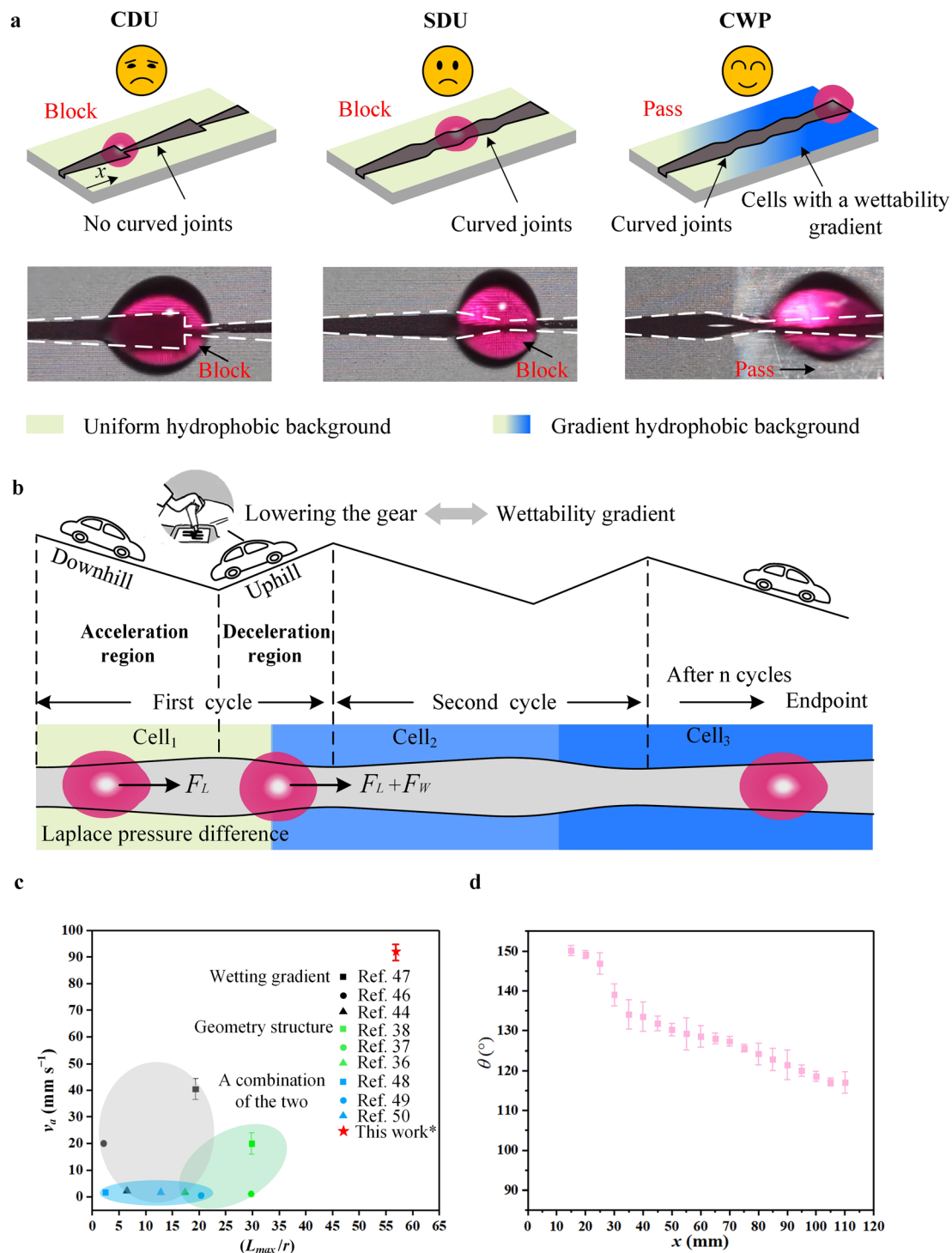
10166 | *J. Mater. Chem. A*, 2023, **11**, 10164–10173

This journal is © The Royal Society of Chemistry 2023

Fig. 1 Design concept of the CDU, SDU, and CWP, motion of a single drop on the CWP, comparison of the transport performance of different surfaces, and wettability of a gradient hydrophobic background. (a) Design concept of the CDU, SDU, and CWP. The drop on the CWP is expected to achieve long-distance transportation owing to the wettability gradient and curved joints of the cells. (b) The motion process of a single drop on the CWP is analogous to that of a car on a periodic downhill and uphill track. The drop is subjected to both the wettability gradient force and the Laplace force at junctions, where the effect of the wettability gradient force is similar to that of lowering the gear of a car at a low speed. (c) Comparison of the transport performance of different surfaces. The green, grey, and blue areas indicate the surfaces with the asymmetric geometry structure, wettability gradient, and combination of the two, respectively. (d) Contact angles θ at different positions along the gradient hydrophobic background with the optimal transportation performance proposed in this study.
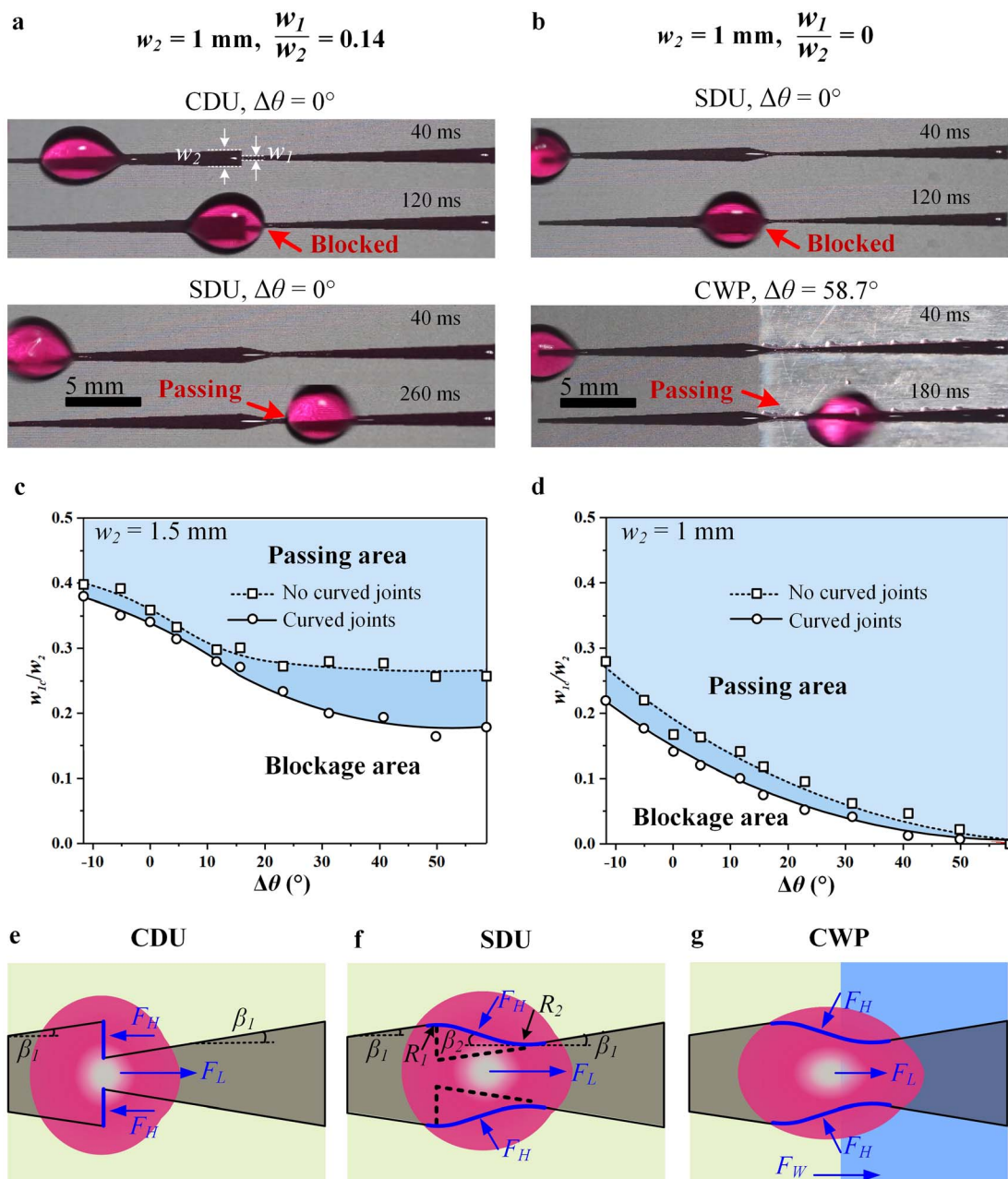
This journal is © The Royal Society of Chemistry 2023

J. Mater. Chem. A, 2023, **11**, 10164–10173 | **10167**

Fig. 2 Effect of the contact angle difference $\Delta\theta$ and the streamlined boundaries of channels with specific β_1 and w_2 values on the motion of a single 25 μL drop at junctions. (a) Transportation processes at CDU ($\Delta\theta = 0°$) and SDU ($\Delta\theta = 0°$) junctions with $\frac{w_1}{w_2} = 0.14$ and $w_2 = 1$ mm showing the drop being blocked and passing, respectively. This implies that the streamlined channel favors the drop passage through junctions. (b) Transportation processes at SDU ($\Delta\theta = 0°$) and CWP ($\Delta\theta = 58.7°$) junctions with $\frac{w_1}{w_2} = 0$ and $w_2 = 1$ mm showing the drop being blocked and passing, respectively. This implies that $\Delta\theta$ favors the drop passage through junctions. (c), (d) relationship between $\frac{w_{1c}}{w_2}$ and $\Delta\theta$ at $w_2 = 1.5$ and 1 mm. The critical w_{1c} means the smallest narrow-side width that can realize the continuous liquid transportation at a given w_2. The results show that the increase in $\Delta\theta$ can reduce the critical width ratio and that both curved joints and a smaller w_2 can increase the size of the passing area, which means that drops can pass through junctions with a small width ratio. (e–g) Force analysis of a single drop located at the CDU, SDU, and CWP junctions. The hysteresis resistance force F_H acts on the blue lines. The curved joint in Fig. 2(f) reduces the hysteresis force component along the transport direction of the drop at the junction compared with the junction in Fig. 2(e). In contrast to the design in Fig. 2(f), the gradient hydrophobic background in Fig. 2(g) causes the drop to be subjected to an additional wettability gradient force at the junction.

10168 | *J. Mater. Chem. A*, 2023, **11**, 10164–10173

This journal is © The Royal Society of Chemistry 2023

channel with streamlined boundaries, the relationship between $\frac{w_{1c}}{w_2}$ and $\Delta\theta$ for $\beta_1 = 0.15°$ and $w_2 = 1$ mm, which is shown in Fig. 2(d), is as follows:

$$\frac{w_{1c}}{w_2} = -0.03 + \frac{589.42}{\left(1 + e^{\left(\frac{\Delta\theta + 276.53}{34.10}\right)}\right)} \quad (-11.6° \leq \Delta\theta \leq 58.7°) \quad (1)$$

We performed the following experiments to verify eqn (1). For a channel with $\Delta\theta = 15.84°$ and $w_2 = 1$ mm, the critical w_{1c} according to the aforementioned equation is around 0.08 mm. We fabricated two samples with $w_1 = 0.1$ mm and $w_1 = 0.06$ mm and found that drops in a channel with $\Delta\theta = 15.84°$, $w_2 = 1$ mm, and $w_1 = 0.1$ mm can cross junctions, while drops in a channel with $\Delta\theta = 15.84°$, $w_2 = 1$ mm, and $w_1 = 0.06$ mm stop at junctions. In addition, when the value of the width ratio is in a certain area of Fig. 2(c) and (d), if drops can pass through junctions, this area is called the "passing area", otherwise it is called the "blockage area". Compared with channels with $w_2 = 1.5$ mm, channels with $w_2 = 1$ mm have a larger passing area, and streamlined boundaries can also play a role in increasing the size of the passing area.

To illustrate the fundamental mechanism of the status of the drop motion at junctions, force analyses were conducted on drops located at CDU, SDU, and CWP junctions. The main driving force for a single drop along a wedge-shaped channel is the Laplace force F_L, which is induced by the curvature gradient and can be expressed as:[55]

$$F_L = \int \frac{d\left[2\gamma_{lg}\sin\theta(x)/w(x)\right]}{dx} S(x) dx \quad (2)$$

where $S(x)$ denotes the cross-sectional area of the droplet, $w(x)$ denotes the channel width, γ_{lg} is the surface tension of the interface between liquid and gas, and $\theta(x)$ is the contact angle of the drop along the boundary between the hydrophobic and hydrophilic regions. In the liquid transportation process, the resistance experienced by the drop is mainly due to the hysteresis resistance force F_H induced by the pinning of contact lines and the viscosity force F_V. However, the latter is small and can thus be ignored because drops move on super-hydrophilic channels after pre-wetting. As shown in Fig. 2(e) and (f), a single drop at the CDU and SDU junctions is subjected to the hysteresis resistance force F_H and the Laplace force F_L. However, compared with the sharp CDU boundaries, the SDU streamlined boundaries with rounded corners lead to a smaller hysteresis resistance force. These boundaries can be simplified to streamlined boundaries without rounded corners, as shown in Fig. S3(a),† and the hysteresis resistance force in the x direction acting at boundaries can be expressed as:[55]
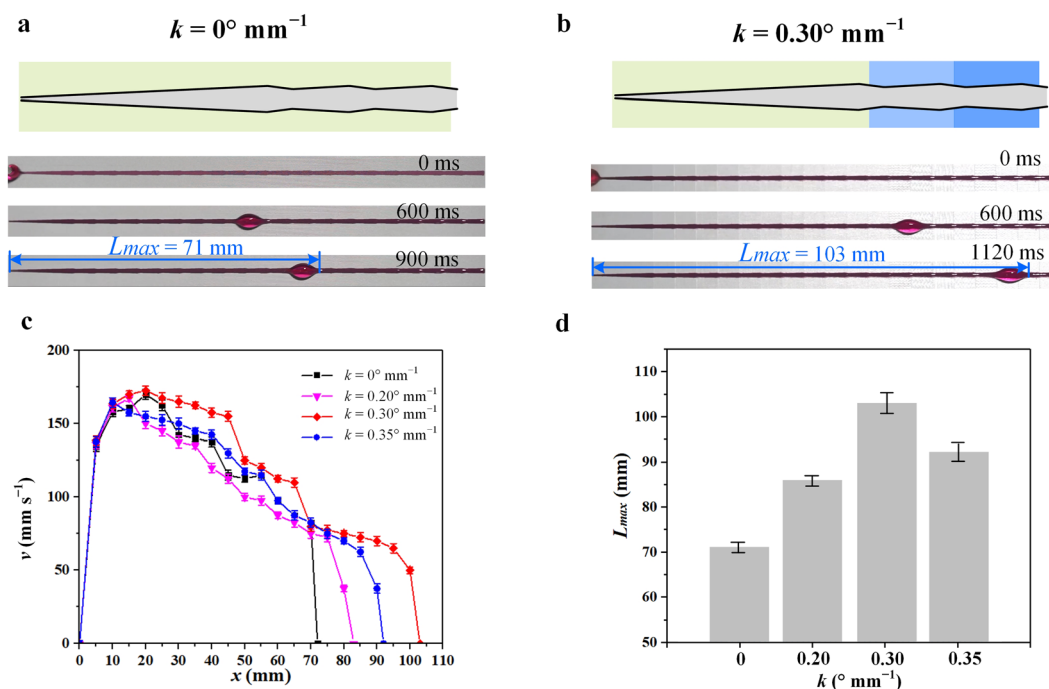

Fig. 3 Transportation processes of a single drop with a volume of 25 μL on different CWPs with different average wettability gradients ($k = 0$, 0.20, 0.30, and 0.35° mm^{-1}). The front end of the drop is the baseline for the measurement of the displacement. (a) Digital images of the transportation process of the drop ($k = 0°$ mm^{-1}). The maximal transportation distance L_{max} is 71 mm. (b) Digital images of the transportation process of the drop ($k = 0.30°$ mm^{-1}). L_{max} is 103 mm. (c) Velocity of the drop at different positions along channels with different gradient hydrophobic backgrounds. For $k = 0.30°$ mm^{-1}, the drop velocity is slightly higher than on other surfaces, and the advantage becomes more pronounced with increasing x. (d) Effect of k on L_{max}. When k exceeds 0.30° mm^{-1}, the value of L_{max} decreases as an increase in k causes an increase in the hysteresis effect. For the CWP with $k = 0.30°$ mm^{-1}, L_{max} reaches its maximum value because there is a sizable wettability gradient in the background without a considerable hysteresis effect.

This journal is © The Royal Society of Chemistry 2023

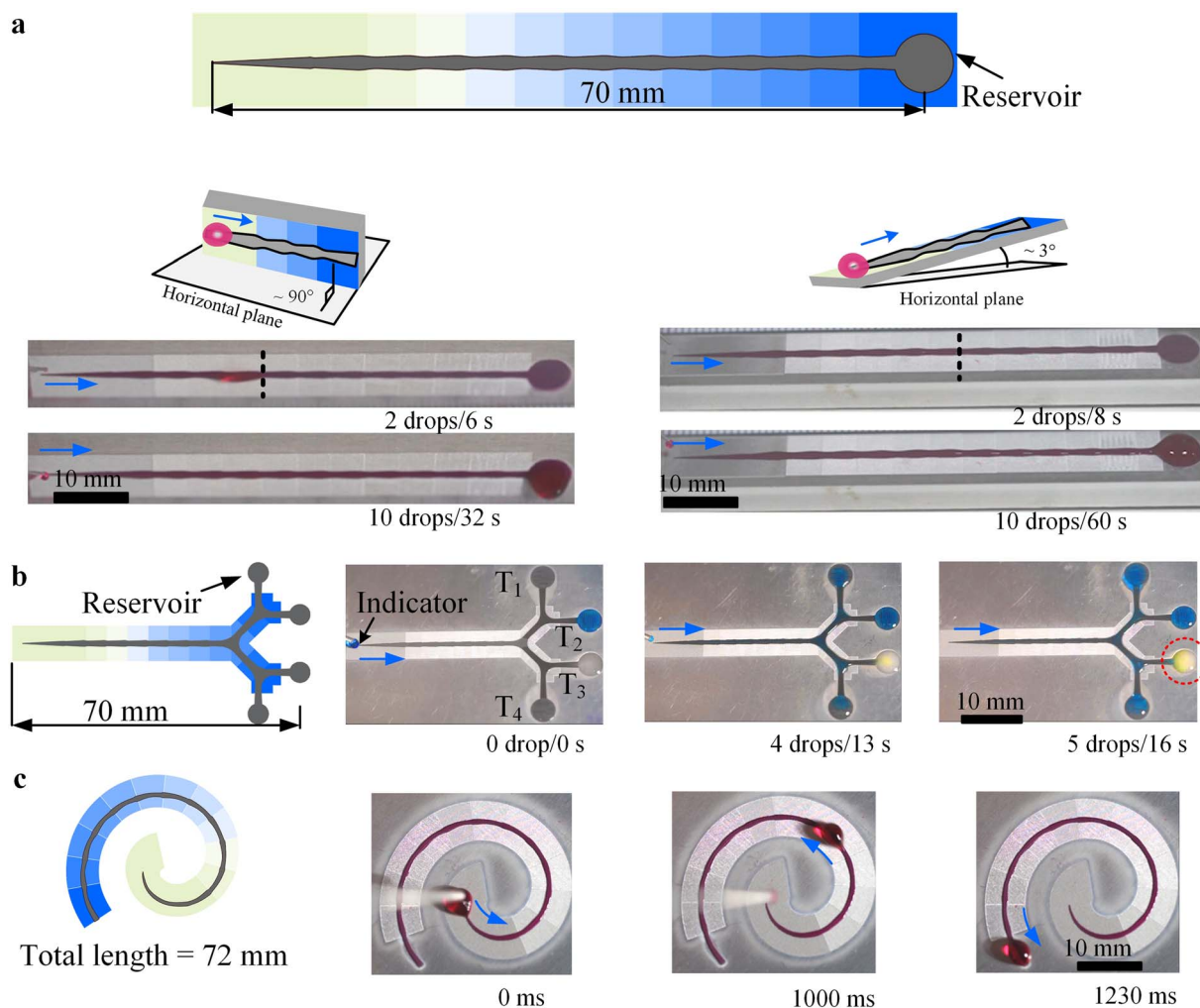J. Mater. Chem. A, 2023, **11**, 10164–10173 | **10169**

Fig. 4 Transportation of drops on different channels. (a) Schematics of the digital images of the continuous transportation of drops (5 μL per drop) along the vertical long-distance straight channel and the inclined straight channel. (b) Digital images of the drop identification process (25 μL per drop) in the horizontal four-reservoir channel. (c) Digital images of the transportation process of a single drop (25 μL) along the horizontal spiral channel.

$$F_H = \gamma_{lg}(w_2 - w_1)\frac{\cos\beta_1\sin\beta_2}{\sin(\beta_1 + \beta_2)}(\cos\theta_a - \cos\theta_r) \quad (3)$$

where θ_a and θ_r are the advancing and receding contact angles, respectively. In addition, the SDU rounded corners can limit the hysteresis effects, as shown in Fig. S3(b1) and (b2).† The hysteresis resistance force in the x direction acting at rounded corners with radius R_1 can be expressed as:

$$F_{Rx} = \int \gamma_{lg}(\cos\theta_a - \cos\theta_r)\cos[\phi(x)]ds$$
$$= \gamma_{lg}(\cos\theta_a - \cos\theta_r)R_1(\cos\beta_2 - \cos\beta_1) \quad (4)$$

where $\varphi(x)$ is the angle between the direction of the surface tension and the positive direction of x, R_1 is the radius of the left side of the rounded corners (see Fig. 2(e)), and ds is the incremental arc length of the left side of the rounded corners. For a single drop at the CWP junction, it is considered that the drop not only contacts the boundary between the hydrophobic region and the hydrophilic region but also partially contacts the

gradient hydrophobic background, as shown in Fig. S3(c1) and (c2).† This leads to the generation of the wettability gradient force F_W due to the imbalance of the surface tension at contact lines, which can be expressed as:[42]

$$F_W = \pi r^2\gamma_{lg}k\sin\theta \quad (5)$$

where r is the base radius of the droplet, and $k = \frac{\Delta\theta}{L}$ is the average wettability gradient (with L being the total background length). As shown in Fig. 2(g), at the CWP junction, the resultant force F can be written as:

$$F = F_W + F_L - F_H \qu(6)$$

Furthermore, for achieving long-distance transportation of drops, the gradient hydrophobic background, which consists of multiple cells with different wettability properties, was used as the substrate, and the influence of the average wettability

10170 | J. Mater. Chem. A, 2023, 11, 10164–10173

This journal is © The Royal Society of Chemistry 2023

gradient k on the drop transportation distance was explored. The transportation processes of a single drop with a volume of 25 μL on different CWPs with different average wettability gradients ($k = 0$, 0.20, 0.30, and 0.35° mm^{-1}) are shown in Video S3,† and the wetting performances at different cells of backgrounds with various k values are presented in Table S5.† The designs of the channels with $k = 0°$ mm^{-1} and $k > 0°$ mm^{-1} are shown in Fig. S4,† and the geometrical parameters of the superhydrophilic channels are listed in Table S4.† As shown in Fig. 3(a) and (b), the drop stops moving on the background with $k = 0.30°$ mm^{-1} at 1120 ms, and L_{max} is 103 mm, which is 45% higher than that obtained at $k = 0°$ mm^{-1} ($L_{max} = 71$ mm) and is the highest among all investigated cases. Furthermore, the average velocity across the whole transportation length v_a can reach 92 mm s^{-1}, which exceeds the value of 79 mm s^{-1} obtained at $k = 0°$ mm^{-1}. In addition, the velocity of the drop at different positions along the CWP with $k = 0.30°$ mm^{-1} is also slightly larger than that on the other CWPs, which confirms the superiority of this surface regarding the droplet speed, as shown in Fig. 3(c). More notably, Fig. 3(d) shows that L_{max} first increases and then decreases with the increase in k. In particular, L_{max} reaches the maximum at $k = 0.30°$ mm^{-1}, and the decrease originates from the hysteresis effect hindering drop motion due to the background. Fig. S5† shows that the values of the sliding angle α and sin α of backgrounds with larger average wettability gradients increase rapidly, which means that the overall dynamic contact performance of backgrounds with larger k is worse. The relationship between sin α and the hysteresis effect is as follows:[56]

$$\frac{mg\sin\alpha}{w} = \gamma_{lg}(\cos\theta_r - \cos\theta_a) \tag{7}$$

where g is the force due to gravity, α is the sliding angle, and m and w are the mass and width of the drop, respectively. From eqn (7), it can be concluded that drops are affected by a larger hysteresis effect on backgrounds with a larger average wettability gradient, which in turn limits their transportation distance. Therefore, L_{max} for the background with $k = 0.30°$ mm^{-1} is the largest as the wettability gradient is sizable and the hysteresis effect generated by the backgrounds is less pronounced.

By combining the streamlined boundaries and gradient hydrophobic backgrounds mentioned above, the capacity of the CWP to continuously transport liquid was further explored. As illustrated in Fig. 4(a) and (b), super-hydrophilic channels with complicated shapes embedded in hydrophobic backgrounds were studied. These channels were composed of streamlined cascaded divergent channels for liquid transportation and reservoirs for liquid collection. The continuous transportation of liquid can be achieved on the vertical long-distance straight channel and the inclined straight channel with a 3° tilt angle, which means liquid can overcome gravity in different directions on the two channels, as shown in Fig. 4(a) as well as Videos S4 and S5.† In addition, liquid identification experiments were performed in the four-reservoir channel, as shown in Fig. 4(b) and Video S6.† During the experiment, a glucose solution (colorless), an indigo carmine solution (blue, Indicator), deionized water (colorless), and a sodium hydroxide solution (colorless, pH > 13) were randomly placed in four reservoirs and labeled T$_1$, T$_2$, T$_3$, and T$_4$ from top to bottom. The color of T$_2$ was blue as the comparison group, which means that T$_2$ is the indigo carmine solution. After five drops of the indicator, the color of T$_3$ became light yellow, while that of the other liquids became blue, which indicates that T$_3$ is the sodium hydroxide solution. This is because a sodium hydroxide solution becomes yellow in a strong alkaline solution.[57] The above results show that the sodium hydroxide solution can be easily identified using the four-reservoir channel. Furthermore, a single drop with a volume of 25 μL can be transported over a distance of 72 mm along the horizontal spiral channel, as shown in Fig. 4(c) and Video S7.†

4. Conclusion

In summary, we developed a cellular design of wettability pattern to achieve ultralong directional drop transportation spontaneously with a high velocity, which is composed of a cascaded super-hydrophilic divergent channel and a gradient hydrophobic background. Specifically, the motion states of individual drops were studied at junctions of channels with various $\Delta\theta$ values, and the effect of different geometric parameters was explored. We found that the drops are subjected to a smaller resistance force at junctions with streamlined boundaries, and $\Delta\theta$ can decrease the critical width ratio $\frac{w_{1c}}{w_2}$, which makes it easier for drops to pass through junctions. Furthermore, we proposed an optimization strategy by adjusting the average wettability gradient k for enhancing the drop transportation distance. The results show that the maximal transportation distance L_{max} can reach 103 mm at $k = 0.30°$ mm^{-1} on a flat plane, which is 45% higher than that obtained at $k = 0°$ mm^{-1}, and the average velocity v_a can reach 92 mm s^{-1}. In addition, the continuous transportation of drops could be achieved conveniently along the vertical long-distance straight channel, inclined straight channel, and horizontal four-reservoir channel. On the other hand, a single drop (25 μL) could be transported over a long-distance along the horizontal spiral channel. In particular, a liquid identification experiment was performed using the four-reservoir channel. It is envisaged that our results will provide a new design concept for liquid transportation, which could be applied to artificial fluid transport systems, water-collecting devices and systems, and biological detection technologies.

Conflicts of interest

There are no conflicts to declare.

Acknowledgements

This journal is © The Royal Society of Chemistry 2023

J. Mater. Chem. A, 2023, **11**, 10164–10173 | **10171**

References

1 Y. Zheng, H. Bai, Z. Huang, X. Tian, F. Q. Nie, Y. Zhao, J. Zhai and L. Jiang, *Nature*, 2010, **463**, 640–643.

2 Y. Q. Luo, F. Song, C. Xu, X. L. Wang and Y. Z. Wang, *Chem. Eng. J.*, 2020, **383**, 123168.

3 W. Q. Lu, R. J. Zhang, S. Toan, R. Xu, F. Y. Zhou, Z. Sun and Z. Q. Sun, *Chem. Eng. J.*, 2022, **429**, 132286.

4 L. Wu, Z. C. Dong, Z. R. Cai, T. Ganapathy, N. X. Fang, C. X. Li, C. L. Yu, Y. Zhang and Y. L. Song, *Nat. Commun.*, 2020, **11**, 521.

5 B. Hu, Z. Duan, B. Xu, K. Zhang, Z. Tang, C. Lu, M. He, L. Jiang and H. Liu, *J. Am. Chem. Soc.*, 2020, **142**, 6111–6116.

6 X. C. Liang, V. Kumar, F. Ahmadi and Y. Y. Zhu, *Droplet*, 2022, **1**, 80–91.

7 X. Leng, L. C. Sun, Y. J. Long and Y. Lu, *Droplet*, 2022, **1**, 139–169.

8 C. L. Gao, L. Wang, Y. C. Lin, J. T. Li, Y. F. Liu, X. Li, S. L. Feng and Y. M. Zheng, *Adv. Funct. Mater.*, 2018, **28**, 1803072.

9 Y. C. Lin, Z. Y. Hu, M. X. Zhang, T. Xu, S. L. Feng, L. Jiang and Y. M. Zheng, *Adv. Funct. Mater.*, 2018, **28**, 1800163.

10 Y. Liu, L. Y. Zhao, J. J. Lin and S. K. Yang, *Sci. Adv.*, 2019, **5**, eaax0380.

11 J. A. Lv, Y. Y. Liu, J. Wei, E. Q. Chen, L. Qin and Y. L. Yu, *Nature*, 2016, **537**, 179–184.

12 Q. Q. Sun, D. H. Wang, Y. N. Li, J. H. Zhang, S. J. Ye, J. X. Cui, L. Q. Chen, Z. K. Wang, H. J. Butt, D. Vollmer and X. Deng, *Nat. Mater.*, 2019, **18**, 936–941.

13 A. Li, H. Z. Li, Z. Li, Z. P. Zhao, K. X. Li, M. Z. Li and Y. L. Song, *Sci. Adv.*, 2020, **6**, eaay5808.

14 X. L. Gou and Z. G. Guo, *Chem. Eng. J.*, 2021, **411**, 128495.

15 H. Chen, P. Zhang, L. Zhang, H. Liu, Y. Jiang, D. Zhang, Z. Han and L. Jiang, *Nature*, 2016, **532**, 85–89.

16 Y. Chen, K. Li, S. Zhang, L. Qin, S. Deng, L. Ge, L. P. Xu, L. Ma, S. Wang and X. Zhang, *ACS Nano*, 2020, **14**, 4654–4661.

17 J. Ju, H. Bai, Y. Zheng, T. Zhao, R. Fang and L. Jiang, *Nat. Commun.*, 2012, **3**, 1247.

18 H. Chen, T. Ran, Y. Gan, J. Zhou, Y. Zhang, L. Zhang, D. Zhang and L. Jiang, *Nat. Mater.*, 2018, **17**, 935–942.

19 X. Yang, J. Song, H. Zheng, X. Deng, X. Liu, X. Lu, J. Sun and D. Zhao, *Lab Chip*, 2017, **17**, 1041–1050.

20 H. Geng, H. Bai, Y. Fan, S. Wang, T. Ba, C. Yu, M. Cao and L. Jiang, *Mater. Horiz.*, 2018, **5**, 303–308.

21 M. K. Chaudhury and G. M. Whitesides, *Science*, 1992, **256**, 1539–1541.

22 S. Chen, Y. Cheng, G. Zhang and Y. W. Zhang, *Nanoscale Adv.*, 2019, **1**, 1175–1180.

23 J. Li, J. Li, J. Sun, S. Feng and Z. Wang, *Adv. Mater.*, 2019, **31**, e1806501.

24 Y. Li, Q. Zhang, R. Chen, Y. Yan, Z. Sun, X. Zhang, D. Tian and L. Jiang, *ACS Nano*, 2021, **15**, 19981–19989.

25 X. Yang, K. Zhuang, Y. Lu and X. Wang, *ACS Nano*, 2021, **15**, 2589–2599.

26 Z. Zhao, H. Li, A. Li, W. Fang, Z. Cai, M. Li, X. Feng and Y. L. Song, *Nat. Commun.*, 2021, **12**, 6899.

27 H. Li, W. Fang, Y. Li, Q. Yang, M. Li, Q. Li, X. Q. Feng and Y. L. Song, *Nat. Commun.*, 2019, **10**, 950.

28 M. He, P. Wang, B. Xu, L. Jiang and H. Liu, *Adv. Funct. Mater.*, 2018, **28**, 1800187.

29 Q. A. Meng, B. Xu, Z. Tang, Y. Wei, L. Jiang and H. Liu, *Adv. Mater. Interfaces*, 2022, **9**, 2101749.

30 P. Wang, R. Bian, Q. A. Meng, H. Liu and L. Jiang, *Adv. Mater.*, 2017, **29**, 1703042.

31 A. Ghosh, R. Ganguly, T. M. Schutzius and C. M. Megaridis, *Lab-on-a-Chip*, 2014, **14**, 1538–1550.

32 D. Gurera and B. Bhushan, *J. Colloid Interface Sci.*, 2019, **551**, 26–38.

33 X. Yu, H. Lai, H. Kang, Y. Liu, Y. Wang and Z. Cheng, *ACS Appl. Mater. Interfaces*, 2022, **14**, 6274–6282.

34 J. Wang, S. Z. Yi, Z. L. Yang, Y. Chen, L. L. Jiang and C. P. Wong, *ACS Appl. Mater. Interfaces*, 2020, **12**, 21080–21087.

35 Q. Q. Wang, Y. He, X. X. Geng, Y. P. Hou and Y. M. Zheng, *ACS Appl. Mater. Interfaces*, 2021, **13**, 48292–48300.

36 G. Buchberger, R. Baumgartner, A. Kogler, T. Fritz, S. Bauer and W. Baumgartner, *Sens. Actuators, A*, 2018, **283**, 375–385.

37 Y. Si, T. Wang, C. Li, C. Yu, N. Li, C. Gao, Z. Dong and L. Jiang, *ACS Nano*, 2018, **12**, 9214–9222.

38 H. Zheng, S. Huang, J. Liu, F. Chen, X. Yang, X. Liu, J. Sun and W. Xu, *Micro Nano Lett.*, 2016, **11**, 269–272.

39 K. Maji, A. Das, M. Dhar and U. Manna, *J. Mater. Chem. A*, 2020, **8**, 25040–25046.

40 A. Shome, A. Das, A. Borbora, M. Dhar and U. Manna, *Chem. Soc. Rev.*, 2022, **51**, 5452–5497.

41 Z. A. Liu, H. Liu, W. Li and J. L. Song, *Chem. Eng. J.*, 2022, **433**, 134568.

42 S. Feng, Q. Wang, Y. Xing, Y. Hou and Y. Zheng, *Adv. Mater. Interfaces*, 2020, **7**, 2000081.

43 S. Lowrey, K. Misiiuk, R. Blaikie and A. Sommers, *Langmuir*, 2022, **38**, 605–619.

44 H. Wu, K. Zhu, B. Cao, Z. Zhang, B. Wu, L. Liang, G. Chai and A. Liu, *Soft Matter*, 2017, **13**, 2995–3002.

45 S. Zhu, J. Li, S. Cai, Y. Bian, C. Chen, B. Xu, Y. Su, Y. Hu, D. Wu and J. Chu, *ACS Appl. Mater. Interfaces*, 2020, **12**, 18110–18115.

46 N. N. Shchedrina, S. I. Kudryashov, M. K. Moskvin, G. V. Odintsova, I. V. Krylach, P. A. Danilov, A. G. Bondarenko, E. A. Davydova, M. I. Fokina, R. O. Olekhnovich, M. V. Uspenskaya and V. P. Veiko, *Opt. Express*, 2021, **29**, 12616–12624.

47 C. Liu, J. Sun, J. Li, C. Xiang, L. Che, Z. Wang and X. Zhou, *Sci. Rep.*, 2017, **7**, 7552.

48 S. Y. Deng, W. F. Shang, S. L. Feng, S. P. Zhu, Y. Xing, D. Li, Y. P. Hou and Y. M. Zheng, *Sci. Rep.*, 2017, **7**, 45687.

49 Y. L. Li, J. M. Huang, J. Cheng, S. P. Xu, P. H. Pi and X. F. Wen, *ACS Appl. Mater. Interfaces*, 2021, **13**, 15857–15865.

50 E. Rossegger, D. Hennen, T. Griesser, I. Roppolo and S. Schlogl, *Polym. Chem.*, 2019, **10**, 1882–1893.

51 R. Feng, F. Song, C. Xu, X. L. Wang and Y. Z. Wang, *Chem. Eng. J.*, 2021, **422**, 130119.

10172 | *J. Mater. Chem. A*, 2023, **11**, 10164–10173

This journal is © The Royal Society of Chemistry 2023

52 U. Sen, S. Chatterjee, R. Ganguly, R. Dodge, L. Yu and C. M. Megaridis, *Langmuir*, 2018, **34**, 1899–1907.

53 X. Wang, J. Zeng, J. Li, X. Yu, Z. Wang and Y. Zhang, *J. Mater. Chem. A*, 2021, **9**, 1507–1516.

54 J. Zhang, F. Chen, Y. Lu, Z. Zhang, J. Liu, Y. Chen, X. Liu, X. Yang, C. J. Carmalt and I. P. Parkin, *J. Mater. Sci.*, 2020, **55**, 498–508.

55 J. L. Song, Z. A. Liu, X. Y. Wang, H. Liu, Y. Lu, X. Deng, C. J. Carmalt and I. P. Parkin, *J. Mater. Chem. A*, 2019, **7**, 13567–13576.

56 D. Oner and T. J. McCarthy, *Abstr. Pap. Am. Chem. Soc.*, 2000, **220**, 7777–7782.

57 A. Wotton, T. Yeung, F. Huang, G. Conibeer, C. Zhao, J. Stride and R. Patterson, *J. Electrochem. Soc.*, 2021, **168**, 044523.